ACS APPLIED MATERIALS & INTERFACES

www.acsami.org

Research Article

Micropyramidal Flexible Ion Gel Sensor for Multianalyte Discrimination and Strain Compensation

Jeongho Lee,[⊥] Quang Trung Le,[⊥] Dawoon Lee, Seonho Nam, Thi Huyen Nguyen, Yongjun Song, Joonsoo Sung, Seung-Woo Son,* and Jaekyun Kim*

Cite This: *ACS Appl. Mater. Interfaces* 2023, 15, 26138−26147

Read Online

ACCESS | Metrics & More | Article Recommendations | Supporting Information

ABSTRACT: A highly sensitive and flexible gas sensor that can detect a wide range of chemicals is crucial for wearable applications. However, conventional single resistance-based flexible sensors face challenges in maintaining chemical sensitivity under mechanical stress and can be affected by interfering gases. This study presents a versatile approach for fabricating a micropyramidal flexible ion gel sensor, which accomplishes sub-ppm sensitivity (<80 ppb) at room temperature and discrimination capability between various analytes, including toluene, isobutylene, ammonia, ethanol, and humidity. The discrimination accuracy of our flexible sensor is as high as 95.86%, enhanced by using machine learning-based algorithms. Moreover, its sensing capability remains stable with only a 2.09% change from the flat state to a 6.5 mm bending radius, further amplifying its universal usage for wearable chemical sensing. Therefore, we envision that a micropyramidal flexible ion gel sensor platform assisted by machine learning-based algorithms will provide a new strategy toward next-generation wearable sensing technology.

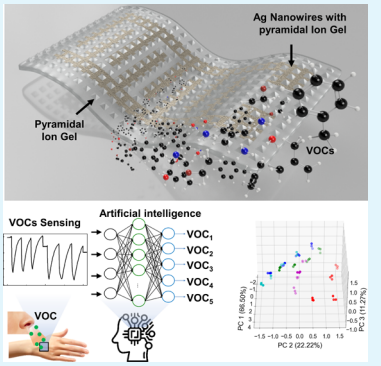

KEYWORDS: *ion gel, VOCs sensor, flexible, machine learning, strain compensation*

1. INTRODUCTION

Flexible electronics have recently fascinated academia and industry due to their emerging applications in health care monitoring, environmental monitoring, Internet-of-Things (IoT), electronic skin, and robotics.[1−4] Rapid industrialization and urbanization in recent decades have also given rise to several environmental issues affecting the quality of air that we breathe in and out daily. Air pollution is a critical problem that harms human and animal health as an invisible poison. Volatile organic compounds (VOCs), commonly used in household products as well as industrial processes, have contributed mainly to air pollution in most indoor places.[5,6] As VOCs can evaporate into the gaseous phase at room temperature, the concentration of indoor VOCs is recorded much higher than that of outdoor VOCs, raising concerns for human health through inhalation and skin contamination.[7] Besides that, ammonia (NH_3) gas is a hazardous substance that harms the human body if exposed to more than the safe level (25 ppm for 8 h or 35 ppm for 10 min). Detecting NH_3 in human breath can also be a biomarker for disease diagnosis.[8,9] Besides detecting VOCs and other toxic gases, monitoring humidity is indispensable in the medical industry and environmental monitoring.[10,11] Therefore, it is necessary to develop sensors detecting multiple analytes.[12] If sensors are flexible, stretchable, and bendable, they can be integrated into wearable applications in various fields.[13,14]

Conventional inorganic material-based sensors are typically fabricated from rigid materials, such as metal, metal oxides, or inorganic semiconductors, restricting the flexibility of devices.[15,16] In addition, the sensing performance of metal oxide material-based gas sensors strongly depends on the working temperature.[17] The TiO_2, SnO_2, CuO, WO_3, and NiO materials have exhibited sensing performance in a wide range of gas concentration detection at a temperature of about 200−500 °C, which is inappropriate for medical, environmental, and indoor sensing applications.[18,19] Two-dimensional (2D) materials, such as graphene, graphene oxide, MXene, and transition metal dichalcogenide monolayers, have been used to fabricate flexible electronic devices.[20−25] A multifunctional self-powered sensor based on MXene/MOF framework-derived CuO performed an excellent response to NH_3 gas with Vg/Va = 24.8 @ 100 ppm.[26] An MXene/NH_2−MWCNT-based formaldehyde sensor showed a great sensing response with an extremely low detection limit (10 ppb).[27] Nonetheless, either growing large-scale 2D materials on flexible substrates or avoiding damage during the transfer process from the initial growth substrate to the target substrate and their stability poses numerous challenges. In addition, the selectivity of 2D materials such as MoS_2 to gases is still limited.[28] Polymers,

Received: February 22, 2023
Accepted: May 8, 2023
Published: May 18, 2023

such as polyethylene terephthalate, polyimide, and poly(dimethylsiloxane), are used as the sensor substrate to perform the flexibility.[29,30] A flexible sensor employing nanocomposite of reduced graphene oxide−tin oxide−poly(vinylidene fluoride) tertiary showed remarkable selectivity to H_2 with a limit of detection of 100 ppb.[31] However, complicated multiprocesses are required to attach the sensing material to those flexible substrates.[32,33] Besides that, the limitation in discriminating multiple analytes with a single sensor platform inhibits the broadening of their practical applications.[34]

Combining ionic liquid (IL) with a polymeric framework to fabricate a free-standing ionic gel structure not only immobilizes the IL but also maintains high ionic conductivity, high thermal and mechanical stability, nonvolatility, and nonflammability.[35,36] Owning to their outstanding properties, IL-based polymer composites have been used in various electronic applications and multidisciplinary sciences.[37,38] 1-Ethyl-3-methylimidazolium bis(trifluoromethyl sulfonyl)imide [$EMIM^+$][$TFSI^-$] was dissolved into dibutyl adipate to fabricate a conductive poly(vinyl chloride) gel-based wearable strain sensor showing excellent electrical and mechanical properties with over 6000 cycles of 100% strain.[39] [$EMIM^+$]-[$TFSI^-$] embedded into the TPU matrix-based sensor exhibited sensitivity with various VOCs and short response times (from 13 to 20 s). However, due to the high hydrophobicity of TPU, the sensitivity to humidity is prohibited.[40] The membrane fabricated from methacrylate-based IL and free IL 1-ethyl-3-methylimidazolium bistriflimide with poly(ethylene glycol) diacrylate (PEGDA) polymerization cross-linker and 2-hydroxy-2-methylpropiophenone (HOMPP) exhibited a remarkable selectivity to gases.[41] The photo-induced radical polymerization approach possesses dominant advantages, especially in the gel formation time, from less than 1 second to a few minutes.

This work presents a flexible ionic gel-based sensor performing multianalyte sensing and strain-compensation capability. The mixture of [$EMIM^+$][$TFSI^-$] ionic liquid, PEGDA monomer, and HOMPP photoinitiator was deposited onto an inverted pyramid silicon mold and was cured with a UV light source. The silver nanowires were introduced as the interdigitated electrode (IDE) structure. The sensor showed a great response to multiple analytes, even at the strain condition. Finally, output signal data were collected, and data processing was performed using machine learning-based algorithms to discriminate the analytes and predict their concentration.

2. MATERIALS AND METHODS

2.1. Material. Silicon wafer ([100], p-type, highly doped) was purchased from ITASCO. Potassium hydroxide (BioXtra, ≥84%, KOH basis), poly(ethylene glycol) diacrylate (average Mn 700, PEGDA), 2-hydroxy-2-methylpropiophenone (97%, HOMPP), and 1-ethyl-3-methylimidazolium bis(trifluoromethylsulfonyl)imide (EMIM, TFSI) were purchased from Sigma−Aldrich. The suspension of AgNWs was purchased from SG FLXIO Co., Ltd.

2.2. Inverted Pyramid Silicon Mold Fabrication. The fabrication of the inverted pyramid silicon mold is depicted in Figure S1 (Supporting Information). A 1.5 cm × 1.5 cm diced silicon substrate was cleaned by sonicating in baths of acetone and isopropanol for 10 min, followed by an oxygen plasma treatment (O_2 flow of 5 sccm, power of 25 W, and working pressure of 5×10^{-1} torr) to eliminate the surface contaminants. The square arrays with a square size of 10 μm × 10 μm and a gap of 10 μm between adjacent patterns were patterned onto the substrate. First, the negative DNR-L300 photoresist was spin-coated onto the silicon substrate at a speed of 3000 rpm for 30 s, followed by soft baking at 90 °C for 60 s. After UV exposure using a conventional contact photolithography system, the pattern was developed by dipping the PR-coated substrate into the AZ 300 MIF Developer for 25 s and then rinsing it under the DI water stream. The successful pattern was confirmed by using an optical microscope. A Cr layer with a thickness of 30 nm was deposited onto the substrate patterned with square arrays as the mask for the etching process using an electron beam evaporator with an evaporation rate of 1.5 Å/s to achieve a continuous and highly dense Cr layer, followed by the lift-off process, which involved dipping the substrate into MR-REM 700 remover solution at 80 °C for 2 h. After the lift-off process, the substrate was immersed in a 30% wt KOH solution at 80 °C for 11 min to perform the etching process and fabricate an inverted pyramid silicon mold. Finally, the Cr layer was removed with a Cr etchant solution.

2.3. Device Fabrication. A stainless steel shadow mask was designed to fabricate the interdigitated electrode structure with an electrode width and distance of 300 μm. The IDE structure of silver nanowires (AgNWs) was deposited onto the pyramid silicon mold using the spray coating method. During the spraying process, the substrate was placed onto the hot plate at 60 °C to accelerate the evaporation rate of the IPA solvent in the AgNW suspension. A premixture of PEGDA and HOMPP (weight ratio of 2:1) was mixed with [$EMIM^+$][$TFSI^-$] ion-pair at varying weight ratios using the stirring bar. Then, the mixture was introduced onto the substrate by drop-casting and stamping with another glass substrate and 55 μm thickness Kapton tape as spacers. UV light curing (354 nm, 150 mJ/cm^2) was exposed to form the ionic gel structure. The glass substrate was then manually peeled off, leaving behind the ionic gel sensor formed under the pyramid structure with the embedded AgNW IDE structure as the electrodes, as shown in Figure S2 (Supporting Information).

2.4. Resistance Measurement for Gas Sensing. The sensing system is illustrated in Figure S3. Target VOCs and nitrogen gas (balance gas) were introduced into the sensing chamber via a mass flow controller (MFC) system with a total flow of 400 sccm. The concentration of target VOCs was calculated based on the following equation

$$[\text{conc}]_{\text{obj}} = \frac{V_{\text{VOC}}}{V_{N_2} + V_{\text{VOC}}} \times [\text{conc}]_{\text{VOC}} \quad (1)$$

where $[\text{conc}]_{\text{obj}}$, $[\text{conc}]_{\text{VOC}}$, V_{VOC}, and V_{N_2} are the objective concentration of VOCs exposed into the sensing chamber, the concentration of VOC gas in the cylinder, the volumetric flow rate of the VOCs, and the volumetric flow rate of the balance N_2 gas, respectively. The relative vapor pressure of VOCs (p/p0) was adjusted by performing the bubbling system mixing the saturated vapor with N_2 gas at the certain ratio determined by the MFC system. N_2 gas was exposed to the chamber to stabilize before the gas-sensing experiment. A certain bias voltage was applied to the sensor, and the resistance change was recorded with a Keithley 2636B source meter mode. The response was defined as follows[42]

$$S = \frac{R - R_0}{R_0} \times 100\% \quad (2)$$

where R and R_0 are the resistance recorded from the sensing device with and without exposing analytes, respectively.

2.5. Data Processing Algorithms. Principal component analysis and random forest-based algorithms in the scikit-learn module were conducted to analyze the extracted sensing data, including concentration, resistance, response curve slopes, response, and gas type.[43] The input data were divided into training and testing datasets (70:30) to evaluate the accuracy of the process. Python v3.8.12 on Visual Studio 2022 was utilized for this process.

https://doi.org/10.1021/acsami.3c02570
ACS Appl. Mater. Interfaces 2023, 15, 26138−26147

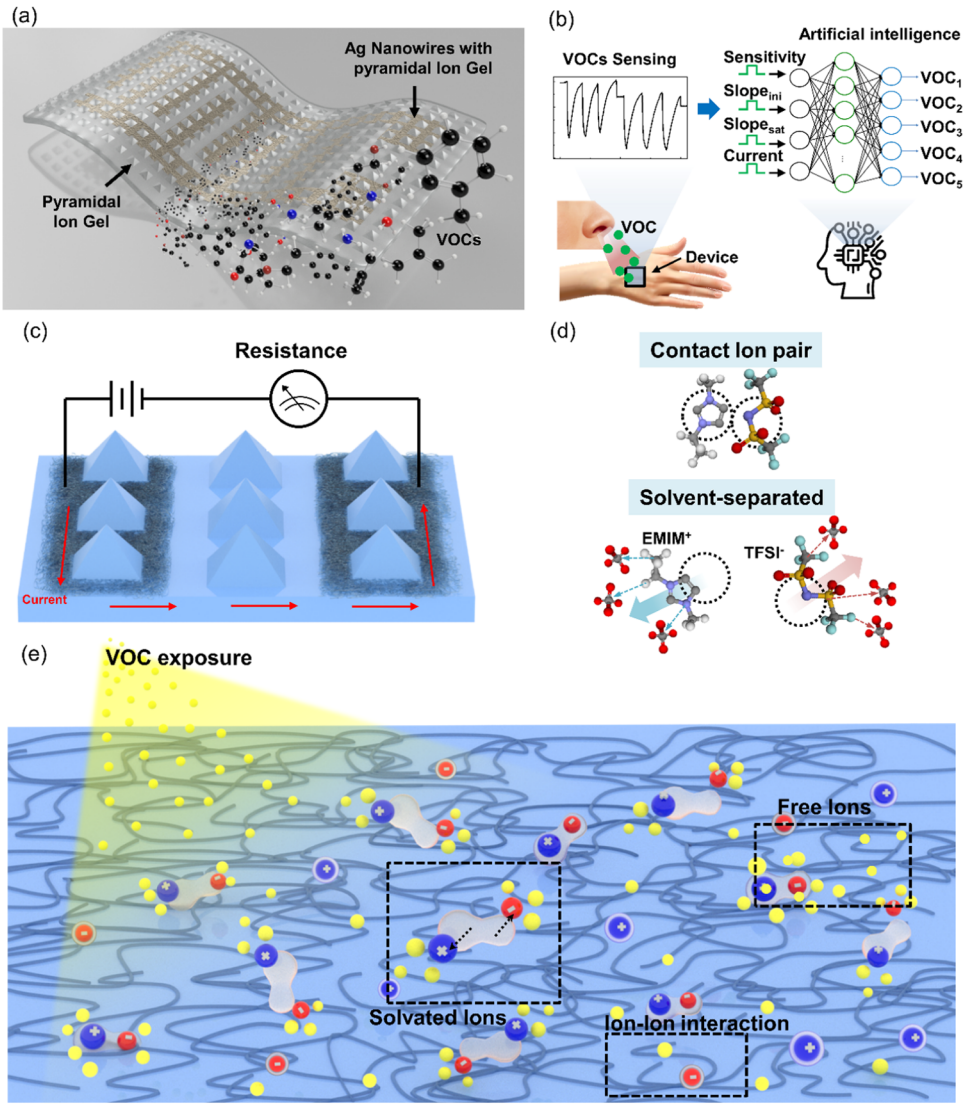

Figure 1. (a) Schematic illustration of a flexible pyramidal structure device with silver nanowire and exposed various VOCs. (b) Prototype of the proposed patched breathanalyzer application with flexible and VOC sensing for a machine learning model. (c) Structural illustration of the pyramidal ionic gel-based sensor. (d, e) Schematic illustration of the working mechanism for the [EMIM$^+$][TFSI$^-$] sensor.

3. RESULTS AND DISCUSSION

3.1. Pyramid Ionic Gel Synthesis, Device Morphology, and Structure Characteristics. Figure 1a shows the schematic illustration of the flexible pyramidal structure-based device fabricated with an ionic gel film and AgNW IDE structure. PEGDA and HOMPP were utilized as a cross-linker and photoinitiator, respectively. [EMIM$^+$][TFSI$^-$] was used as an ionic liquid of the ionic gel due to the high mobility of EMIM$^+$.[44] [EMIM$^+$][TFSI$^-$] with various weight compositions from 10% to 70% was added to the prepared mixture of PEGDA and HOMPP (2:1). Under ultraviolet (UV) exposure, the flexibly patterned structure shape with PEGDA and HOMPP can be maintained, as depicted in Figure 2a. In addition, the IDE structure was introduced with AgNWs (about 25 μm in length) to maintain the elastic properties of the overall structure. AgNWs were spray-coated onto the inverted pyramid silicon mold to produce the IDE electrodes, as shown in Figure 2a,b. After drop-casting the ionic gel onto the AgNW IDE electrode, the electrolyte was patterned with UV irradiation. The thickness of the ionic gel layer was controlled through the Kapton tape spacer and the stamping glass. The pyramid array of patterned ionic gel was successfully fabricated in the areas with and without the AgNW IDE structure, as shown in Figure 2c–f. Due to outstanding conductivity and bendability, AgNW material was utilized to fabricate electrodes in flexible electronics.[45,46] As can be seen in Figure 2d, the free-standing pyramidal ionic gel sensor was bent on an optical fiber with a radius of 400 μm, indicating the great flexibility of the device. SEM and AFM images depicted in Figures S4a–d and S5, respectively, show the uniform pyramid structure with a length and width of 10 μm and a height of 7 μm, approximately. Figure 2e,f shows the SEM images of the pyramid structure in the area with and without AgNWs, respectively. As shown in Figure 2e, the AgNWs were embedded into the ionic gel structure at the micropyramidal structure area, while outside the micropyramidal structure, the AgNWs were partially covered on the ionic gel surface. In addition, Figure 2f exhibits the rugged surface of the micropyramidal structure. Therefore, the analyte adsorption area is further enlarged.

https://doi.org/10.1021/acsami.3c02570
ACS Appl. Mater. Interfaces 2023, 15, 26138−26147

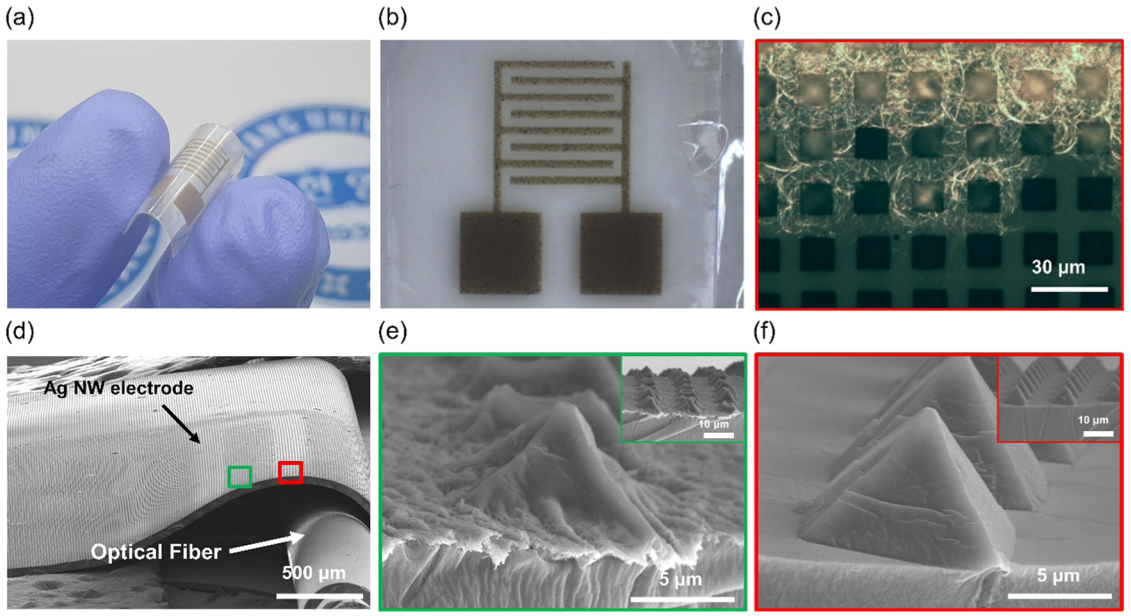

Figure 2. (a) Digital image of the sensor device. (b–c) Microscopic images. (d–f) FE-SEM images were obtained from the fracture of the flexible ion-gel film with a silver nanowire and assisted optical fiber of 40 μm.

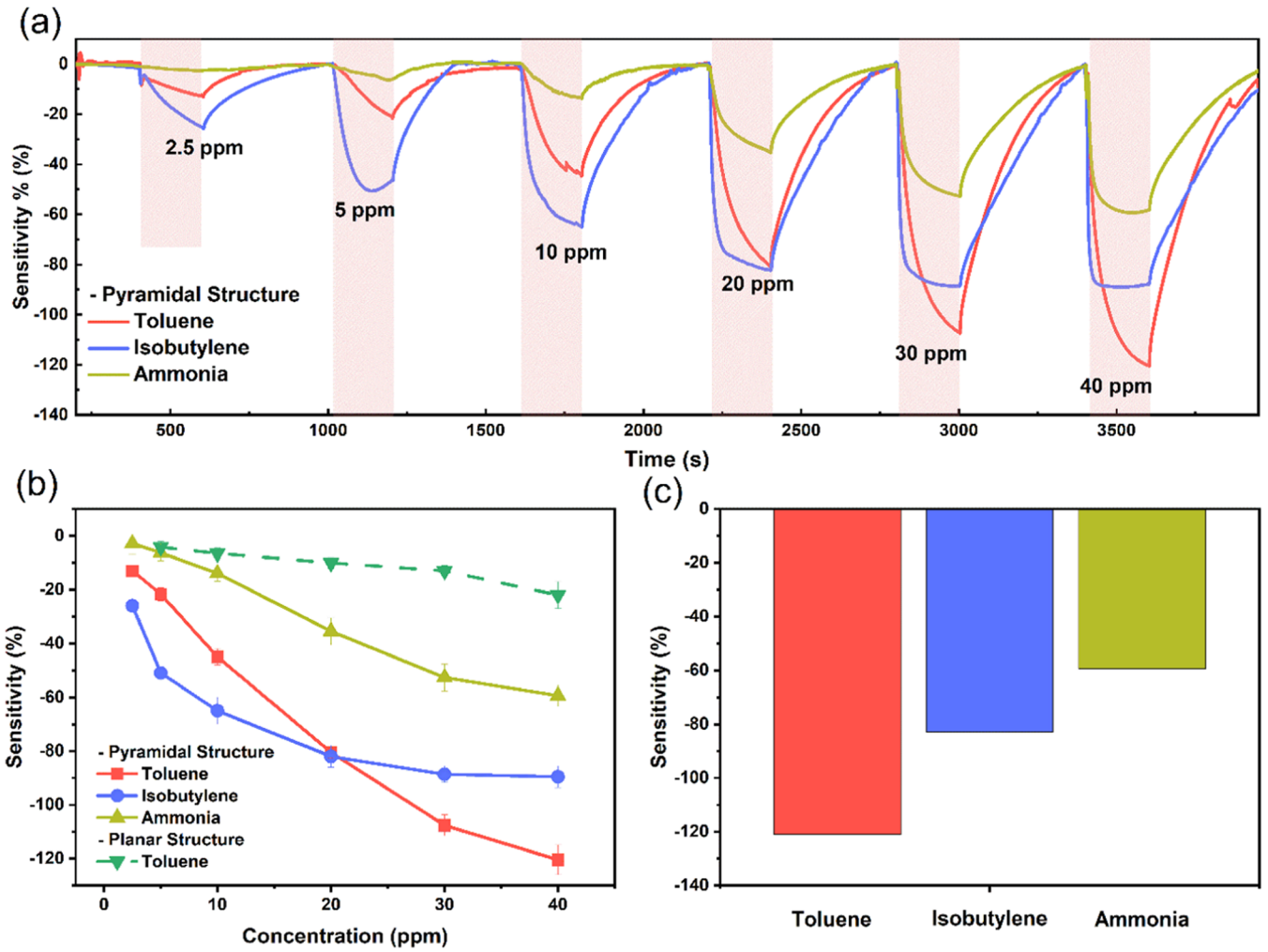

Figure 3. (a, b) Response of the sensor to gases at room temperature. (c) Selectivity of the sensor to gases at 40 ppm.

https://doi.org/10.1021/acsami.3c02570
ACS Appl. Mater. Interfaces 2023, 15, 26138–26147

In addition, surface functional groups of samples were characterized via FT-IR analysis. The FT-IR spectra of [EMIM$^+$][TFSI$^-$] liquid and ionic gel samples at room temperature with the ratio of ionic liquid from 0 to 70% are shown in Figure S6a. The [EMIM$^+$][TFSI$^-$] liquid spectra depict strong adsorption bands due to the mode of in-plane imidazole stretching and CH_3(N) stretching (1574 cm^{-1}),[47] O−S−O stretching (1350 cm^{-1}), C-ethyl (methyl) stretching (1183 cm^{-1}), CF_3 stretching (1132 cm^{-1}), S−N−S stretching (1054 cm^{-1}),[48] H−C−C−H bending and C−S stretching (790 cm^{-1}), CF_3 and CH_3 bending (738 cm^{-1}),[47] and O−S−O antisymmetric bending (613 cm^{-1}).[49] Besides that, the adsorption bands of PEGDA and HOMPP (0% of IL) attributed to −CH stretching (2868 cm^{-1}), C═O stretching (1731 cm^{-1}), C═C symmetric stretching (1676 cm^{-1}), C═CH2 twisting (1446 cm^{-1}), and C−O−C bonding (1094 cm^{-1}).[50] There is no peak at about 800 and 1400 cm^{-1}, indicating the high degree of polymerization of PEGDA.[51] The weak adsorption peak of [EMIM$^+$][TFSI$^-$] at 3162 cm^{-1} is attributed to the aliphatic C−H modes of the CH_3 group bonded to the [EMIM] ring. The peak at 2980 cm^{-1} is due to the C−H stretching modes of C atoms in the ring.[50] As can be seen in Figure S6b, the adsorption intensities of [EMIM$^+$]-[TFSI$^-$] vibrational modes increase with the increase of the ILs ratio in the fabrication components (0−70%).

3.2. Gas-Sensing Performance of Ionic Gel Sensors. The response of the ionic gel sensor is determined by observing the relative resistance variation ($\Delta R/R_0$) of the sensor upon exposure to the analytes at room temperature. R_0 and ΔR represent the resistance in a pure N_2 stream and the resistance change with the exposure of analytes, respectively. Figure S7a exhibits the response of sensors fabricated from different IL component ratios (10−70%, wt) with various applied bias voltages (1−1.75 V). With the increase of the IL ratio, the response of the sensor to gas tends to increase and reach the peak at 50% ILs as the number of ions is sufficient. Then the response decreases with the increase of ILs to 70% due to the low viscosity of the ionic gel.[52] The sample with 50% ILs exhibits the highest response at the applied bias voltage of 1.5 V. Hence, the sensor with 50% ILs was used for further investigations. Besides that, a planar ionic gel sensor without the pyramidal structure was fabricated as the reference sample to determine the enhancement of the pyramidal structure in gas-sensing performance. As shown in Figure S7b, the sensor exhibits a negative response to gas exposure. The planar structure-based sensor performs a response of 18% to toluene 40 ppm, while the pyramidal structure-based sensor performs 80%, indicating the enhancement of the pyramidal structure to gas-sensing performance. With the pyramidal structure, the sensing surface area exposed to gases is significantly widened, enhancing the absorption of gas molecules into the ionic gel. Consequently, the response of the sensor was improved. Notably, AgNWs could not perform the sensing ability to gases with a concentration below 3%.[53] Therefore, AgNWs merely play the role of the electrodes and have a negligible contribution to the gas-sensing performance of the device.

Figures 3a and S8 show the dynamic response of the ionic gel sensor to different concentrations of toluene, isobutylene, ammonia, ethanol, and humidity at room temperature. The negative resistance variations of the sensor were observed during the exposure to gases. The response tends to increase gradually with the increase of gas concentrations from 2.5 to 40 ppm, as shown in Figure 3b. The sensor exhibits linear responses to toluene and ammonia gas concentration up to 30 ppm, and then the responses tend to be saturated. Figure S8 shows the response of the sensor to ethanol and humidity at different concentrations (in the range of 2.4−76 ppm), which are formed using a bubbler system, and the exposure concentration was confirmed using a commercial sensor (BME680; Bosch). The resistance decreases with the increase in relative humidity, which is consistent with the previous report.[35] As a large number of water molecules are introduced, the sensor displays saturation behavior with analyte concentrations over 40%. As shown in Figure S9, the response curves of the sensor to toluene and ammonia can be expressed as the linear regression mathematical equation of $y = 3.4098x + 6.4001$ and $y = 1.6039x - 1.1518$, respectively, where y and x are the response of the sensor and the concentration of gases, respectively. The limit of detection (LOD) can be determined as LOD = 3 × (No/S), where No = 0.0392 and S are the noise and the slope of the curve, respectively (Figure S9, Table S1, and Supporting text).[54,55] The calculated LODs of the sensor in toluene and ammonia detection are 34 and 73 ppb, respectively. These susceptible responses of the ionic gel sensor indicate the capability of detecting gases in the environment. Moreover, the exceptional resilience of the resistance parameter by exposing balance gas (N_2) after introducing analytes demonstrates the high reliability of the sensor. However, as depicted in Figure S10, the stability of the ionic gel sensor gradually decreases with time. The sensing performance decreased by about 20% after 7 days of storage in the ambient condition. It can be attributed to the absorption of ambient gases and the oxidization of AgNWs in the ambient environment. In addition, the selectivity of the ionic gel sensor commonly determined by comparing the response of the sensor to gases, as depicted in Figure 3c, is low, in consistency with the previous study.[40] Hence, further work is crucial in order to improve the selectivity performance of the ionic gel sensor.

3.3. Selectivity Enhancement with Principal Component Analysis and Random Forest Classifier. Artificial intelligence techniques were used to improve the selectivity of the ionic gel sensor. Data were extracted from the sensing curve of the sensor for analytes, including response, initial slope, saturated slope, electrical current, exposed gas concentration, and gas type. The absorption of different analytes by the sensing material strongly depends on their chemical and physical characteristics. The typical approach to determining the selectivity is commonly based on the maximum change in resistance or conductance of the sensor toward analytes. Since this feature exhibited a low importance weight compared with other coefficients of the response curves, the selectivity based on the maximum change in resistance is inadequate. The features related to the analyte adsorption period showed a four-order higher importance weight than the maximum change in resistance in terms of analyte discrimination using machine learning algorithms. The slopes of the response curves at the analyte adsorption period not only are the alternative features of those fitting coefficients but also simplify the process using the exponential fitting method.[56] Therefore, the relationship between response, slopes, and other parameters is valuable information that can be used to discriminate analytes. The principal component analysis (PCA) technique performs the dimensional reduction process. Figure 4a,b shows the correlation between compo-

https://doi.org/10.1021/acsami.3c02570
ACS Appl. Mater. Interfaces 2023, 15, 26138−26147

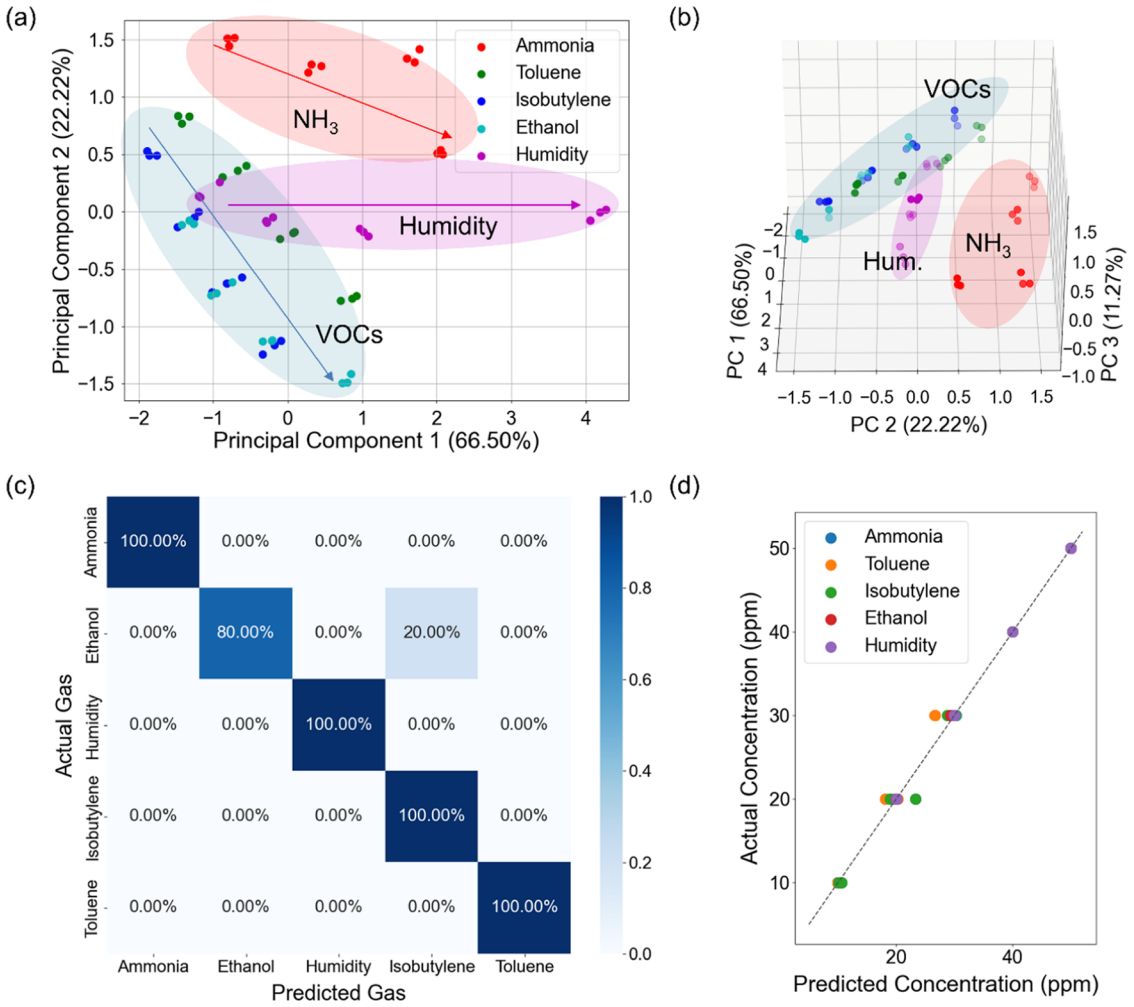

Figure 4. (a, b) 2D and 3D principal component analysis plots, respectively. (c) Normalized confusion matrix of a random forest classifier and (d) gas concentration detection.

nents corresponding to gases. In the two-dimensional PCA plot, the scattering of ammonia gas has a top-left to right-bottom orientation with increasing gas concentration, humidity is located in a left-to-right orientation, while the scattering of VOC gases (toluene, isobutylene, and ethanol) is distributed in a different direction. As can be seen in the three-dimensional PCA plot, the scattering areas of ammonia, humidity, and VOC group are distinguishable.

Subsequently, random forest classifier and regressor algorithms were used to improve selectivity and predict gas concentration. Random forest is a multiadvantage, high-accuracy machine learning-based classifier integrated into a single sensor platform.[57,58] Figure 4c exhibits the confusion matrix result from the random forest classifier algorithm analysis. The sensor integrated with machine learning can classify various analytes (ammonia, ethanol, humidity, isobutylene, and toluene) with accuracy scores of 95.86%. Besides that, Figure 4d demonstrates the high accuracy of the prediction (92.35%). Most points indicating the predicted concentration versus the actual concentration are scattered along the diagonal line. Since the chemical and physical characteristics of analytes strongly impact their adsorption and desorption behavior through mass, adsorption, and desorption activation energy of analytes,[56] extracting the adsorption/desorption information through the curve slopes and the other parameters is worth data to enhance the selectivity feature of the sensor. The results express the automatic detection and prediction capability of the sensor without human operation.

3.4. Flexible and Strain-Compensated VOC Sensing.

Figure 5a depicts the resistance change of the ionic gel sensor to cyclic bending of the sensor at different radii, from 15 to 6.5 mm. The experiment was conducted at ambient conditions with a temperature of 25 °C and a humidity of 50%. The negative resistance changes increase from 21% to 94% with decreases in the bending radius from 15 to 6.5 mm, respectively, as shown in Figure 5b. Besides that, remarkable resilience is observed after releasing the sensor back to its original state. In order to evaluate the strain-compensation performance of the sensor, the resistance change of the sensor was recorded with the human exhaling breath under a bending state at different radii and compared with the initial flat state. The human exhaling contains high humidity, resulting in a negative resistance change, as exhibited in Figure 5c. The background resistance gradually increases with the decrease in bending radius, as depicted by the blue dashed line in Figure 5c, which is consistent with the results shown in Figure 5a. The response of the sensor to the analyte is not related to the bending radius, as shown in Figure 5d. The response of the sensor in bending status is almost the same as the flat state by

https://doi.org/10.1021/acsami.3c02570
ACS Appl. Mater. Interfaces 2023, 15, 26138−26147

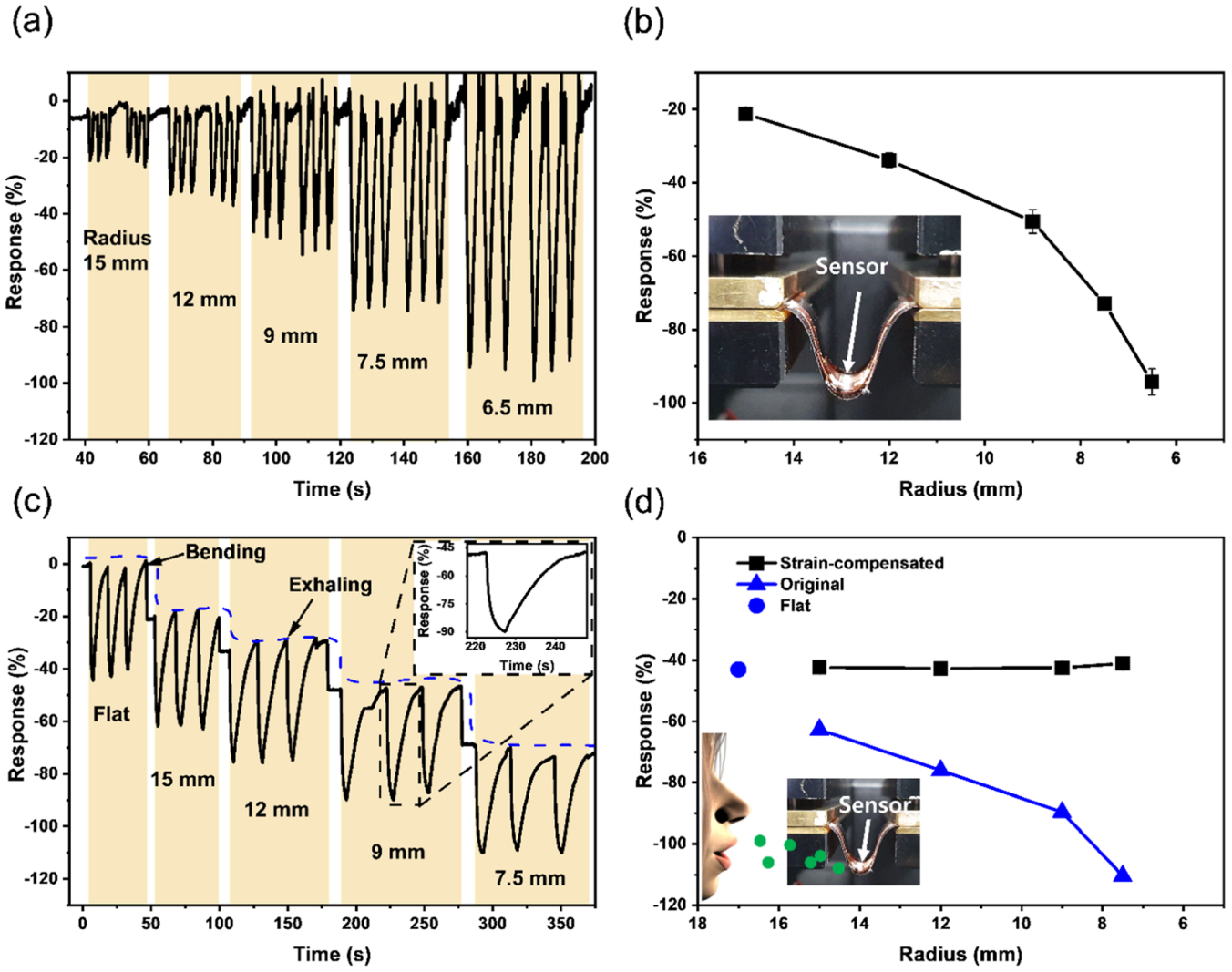

Figure 5. (a) Real-time strain-response of narrow radius from 15 to 6.5 mm. (b) Resistance change with different bending radii. (c) Response and strain-response of narrow radius from 15 to 7.5 mm for exhale sensing in ambient conditions. Inset is the zoom-in of the exhaling curve. (d) Comparison of response at various radii to human exhaling breath with and without strain compensation (room temperature: 25 °C, relative humidity: 50%).

the compensation. The results indicate the effectiveness of the sensor in bending strain-compensation performance.

In order to determine the response of the sensor in actual environmental conditions, an experiment monitoring ethanol in exhaling breath was conducted at ambient conditions. Ethanol with different concentrations (from 0 to 30%) was prepared. As depicted in Figure S12, the response was recorded during exhaling after gargling with prepared ethanol solutions.[59] The response gradually increases from 40 to 56% with the increase in ethanol concentration from 0 to 30%, respectively. As shown in Figure S12c,d, the slope of the slow-response region increases with the increase in ethanol concentration in exhaling breath. The sensor exhibits the lowest response but the highest saturation speed at an ethanol concentration of 0%. The increase in the slope of the slow-response region is consistent with the response time exhibited in Figure S12e. At low concentrations of ethanol, the sensor quickly reaches the saturation value. Without ethanol (concentration of 0%), the sensor reaches saturation value after about 2 s, while at the concentration of 30%, it takes about 6.5 s, indicating that more time is necessary to dissolve gas molecules at higher concentrations into the IL. In addition, Figure S12e also depicts the recovery time of the sensor after exposure to ethanol in the exhaling breath. The recovery time increases with the increase in ethanol concentration.

3.5. Sensing Mechanism. When the sensor is exposed to analytes, negative responses are recorded due to the increase in conductance of the sensor. The sensing mechanism of the ion gel sensor is based on the miscibility of the analytes into the ILs. Interactions such as dipole orientation, induction, or hydrogen bonding can simultaneously occur, thereby affecting the physicochemical characteristics of the ILs.[60] Among others, IL viscosity change is the most relevant factor directly resulting in conductivity, diffusion coefficient, and charge transfer rate changes. The relationship between conductivity and viscosity is shown in the following equation[61]

$$\sigma = \frac{yF^2d}{6\pi N_A FW} \frac{[(\zeta_c r_c)^{-1} + (\zeta_a r_a)^{-1}]}{\eta} \quad (3)$$

where σ and η are conductivity and viscosity, respectively. N_A, r_a, r_c, ζ_a, ζ_c, FW, F, and d are the Avogadro number, the anion and cation radius, the microviscosity factors, formula weight,

https://doi.org/10.1021/acsami.3c02570
ACS Appl. Mater. Interfaces 2023, 15, 26138−26147

Faraday constant, and density, respectively. Equation 3 exhibits the inverse proportional dependence between the conductivity σ and the viscosity η of ILs. Besides that, the Seddon's equation shows the change in viscosity of ILs after dissolving gases as follows[62]

$$\eta = \eta_s \exp\left(-\frac{\chi_{cs}}{a}\right) \quad (4)$$

where η, η_s, χ_{cs}, and a are the viscosity of the pure IL and gas-dissolved IL at 20 °C, the mole fraction of the dissolved gas, and the constant for specific IL, respectively. When IL absorbs gas, the dissolved gas molecules prevent ions from interacting, reducing IL viscosity and increasing the number of free ions, as depicted in Figure 1e. Consequently, the conductivity rises with gas exposure.

In situ FTIR spectra of the ionic gel exposed to ethanol for different durations were recorded, as depicted in Figure S13. The O−H stretching vibrational mode in the wavenumber area of about 3500 cm^{-1}, the C−H stretching mode at 2974 and 2874 cm^{-1} peak intensity enhancements, and the appearance of a new peak of the C−C−O symmetric stretching vibrational mode at the wavenumber of 879 cm^{-1} indicate the absorption of ethanol molecules into IL.[63] Besides that, the peak intensity decreases at the wavenumbers of 1350, 1333, 1134, 1056, 789 cm^{-1} (correlated to [EMIM]), 1184 and 850 cm^{-1} (correlated to [TFSI]),[47−49] indicating the solvation of [$EMIM^+$][$TFSI^-$]. As ethanol molecules dissolve, enhance the ion solvation, and inhibit the interaction between ions, the peak intensity of [$EMIM^+$][$TFSI^-$] decreases.[64,65]

4. CONCLUSIONS

In summary, the flexible pyramidal structure-based sensor has been fabricated with [$EMIM^+$][$TFSI^-$] ionic gel, PEGDA, and HOMPP as a cross-linker and photoinitiator, respectively. The sample with ILs 50% shows a more extraordinary sensing performance than the lower or higher IL components. The sensor exhibits a susceptible response to analytes such as ammonia, toluene, isobutylene, ethanol, and water, with linear responses in the concentration range of 2.5−40 ppm at room temperature. The limit of detection is estimated at 30−80 ppb. The response time is about 2−6.5 s. The selectivity of the sensor to analytes is carried out using principal component analysis and random forest-based algorithms with high accuracy of over 95%. Subsequently, the analyte concentration is predicted with an accuracy of over 92%. In addition, the sensor exhibits effectiveness in bending strain-compensation performance with bending radii in the range of 15−6.5 mm. The sensitive response of the sensor (39.8−56.4%) detects ethanol in exhaling breath with concentrations of 0−30%, indicating the practical application potential of the micro-pyramidal flexible ion gel sensor platform. In future work, the simultaneous exposure of analytes and structural deformation will be investigated to enhance the practical application of the ionic gel sensors.

■ ASSOCIATED CONTENT

Supporting Information

The Supporting Information is available free of charge at https://pubs.acs.org/doi/10.1021/acsami.3c02570.

Sample preparation; additional SEM, AFM, FTIR measurement; additional sensing measurement; limit of detection (LOD) calculation method (PDF)

■ AUTHOR INFORMATION

Corresponding Authors

Seung-Woo Son − *Department of Applied Physics and Department of Applied Artificial Intelligence, Hanyang University, Ansan, Gyeonggi 15888, Republic of Korea*; Email: sonswoo@hanyang.ac.kr

Jaekyun Kim − *Department of Photonics and Nanoelectronics, Hanyang University, Ansan, Gyeonggi 15888, Republic of Korea; BK21 FOUR ERICA-ACE Center, Hanyang University, Ansan, Gyeonggi 15588, Republic of Korea*; Email: jaekyunkim@hanyang.ac.kr

Authors

Jeongho Lee − *Department of Photonics and Nanoelectronics, Hanyang University, Ansan, Gyeonggi 15888, Republic of Korea; BK21 FOUR ERICA-ACE Center, Hanyang University, Ansan, Gyeonggi 15588, Republic of Korea*; orcid.org/0000-0002-6704-250X

Quang Trung Le − *Department of Photonics and Nanoelectronics, Hanyang University, Ansan, Gyeonggi 15888, Republic of Korea; BK21 FOUR ERICA-ACE Center, Hanyang University, Ansan, Gyeonggi 15588, Republic of Korea*; orcid.org/0000-0002-2032-3523

Dawoon Lee − *Department of Photonics and Nanoelectronics, Hanyang University, Ansan, Gyeonggi 15888, Republic of Korea*; orcid.org/0000-0003-4386-9278

Seonho Nam − *Department of Applied Physics, Hanyang University, Ansan, Gyeonggi 15888, Republic of Korea*

Thi Huyen Nguyen − *Department of Photonics and Nanoelectronics, Hanyang University, Ansan, Gyeonggi 15888, Republic of Korea; BK21 FOUR ERICA-ACE Center, Hanyang University, Ansan, Gyeonggi 15588, Republic of Korea*

Yongjun Song − *Department of Photonics and Nanoelectronics, Hanyang University, Ansan, Gyeonggi 15888, Republic of Korea; BK21 FOUR ERICA-ACE Center, Hanyang University, Ansan, Gyeonggi 15588, Republic of Korea*

Joonsoo Sung − *Department of Photonics and Nanoelectronics, Hanyang University, Ansan, Gyeonggi 15888, Republic of Korea; BK21 FOUR ERICA-ACE Center, Hanyang University, Ansan, Gyeonggi 15588, Republic of Korea*

Complete contact information is available at: https://pubs.acs.org/10.1021/acsami.3c02570

Author Contributions

[⊥]J.L. and Q.T.L. contributed equally to this work. The manuscript was written through contributions of all authors. All authors have given approval to the final version of the manuscript.

Notes

The authors declare no competing financial interest.

■ ACKNOWLEDGMENTS

This research was supported by the Korea Basic Science Institute (National Research Facilities and Equipment Center) grant funded by the Ministry of Education (Grant No. 2021R1A6C101A405), Korea National Research Foundation (NRF) (Grant Nos 2023R1A2C1007034 and 2020R1A2C2010875), Hanyang University, the Institute of Information & Communications Technology Planning &

Evaluation (IITP) grant funded by the Korea government (MSIT) (Grant No. RS-2022-00155885, and Artificial Intelligence Convergence Innovation Human Resources Development (Hanyang University ERICA)) (S.-W.S.).

REFERENCES

(1) Kim, D. C.; Shim, H. J.; Lee, W.; Koo, J. H.; Kim, D. H. Material-Based Approaches for the Fabrication of Stretchable Electronics. *Adv. Mater.* **2020**, *32*, No. e1902743.
(2) Huang, Q.; Zhu, Y. Printing Conductive Nanomaterials for Flexible and Stretchable Electronics: A Review of Materials, Processes, and Applications. *Adv. Mater. Technol.* **2019**, *4*, No. 1800546.
(3) Zhai, K.; Wang, H.; Ding, Q.; Wu, Z.; Ding, M.; Tao, K.; Yang, B. R.; Xie, X.; Li, C.; Wu, J. High-Performance Strain Sensors Based on Organohydrogel Microsphere Film for Wearable Human-Computer Interfacing. *Adv. Sci.* **2023**, *10*, No. e2205632.
(4) Chen, J.; Zhu, G.; Wang, J.; Chang, X.; Zhu, Y. Multifunctional Iontronic Sensor Based on Liquid Metal-Filled Hollow Ionogel Fibers in Detecting Pressure, Temperature, and Proximity. *ACS Appl. Mater. Interfaces* **2023**, *15*, 7485−7495.
(5) Badol, C.; Locoge, N.; Leonardis, T.; Galloo, J. C. Using a Source-Receptor Approach to Characterise Voc Behaviour in a French Urban Area Influenced by Industrial Emissions. Part I: Study Area Description, Data Set Acquisition and Qualitative Data Analysis of the Data Set. *Sci. Total. Environ.* **2008**, *389*, 441−452.
(6) Guarnieri, M.; Balmes, J. R. Outdoor Air Pollution and Asthma. *Lancet* **2014**, *383*, 1581−1592.
(7) Heeley-Hill, A. C.; Grange, S. K.; Ward, M. W.; Lewis, A. C.; Owen, N.; Jordan, C.; Hodgson, G.; Adamson, G. Frequency of Use of Household Products Containing VOCs and Indoor Atmospheric Concentrations in Homes. *Environ. Sci.: Process Impacts* **2021**, *23*, 699−713.
(8) Ricci, P. P.; Gregory, O. J. Sensors for the Detection of Ammonia as a Potential Biomarker for Health Screening. *Sci. Rep.* **2021**, *11*, No. 7185.
(9) Das, S.; Pal, M. Review—Non-Invasive Monitoring of Human Health by Exhaled Breath Analysis: A Comprehensive Review. *J. Electrochem. Soc.* **2020**, *167*, No. 037562.
(10) Duan, Z.; Jiang, Y.; Yan, M.; Wang, S.; Yuan, Z.; Zhao, Q.; Sun, P.; Xie, G.; Du, X.; Tai, H. Facile, Flexible, Cost-Saving, and Environment-Friendly Paper-Based Humidity Sensor for Multifunctional Applications. *ACS Appl. Mater. Interfaces* **2019**, *11*, 21840−21849.
(11) Ding, Q.; Wang, H.; Zhou, Z.; Wu, Z.; Tao, K.; Gui, X.; Liu, C.; Shi, W.; Wu, J. Stretchable, Self-Healable, and Breathable Biomimetic Iontronics with Superior Humidity-Sensing Performance for Wireless Respiration Monitoring. *SmartMat* **2023**, *4*, No. e1147.
(12) Park, J.; Tabata, H. Gas Sensor Array Using a Hybrid Structure Based on Zeolite and Oxide Semiconductors for Multiple Bio-Gas Detection. *ACS Omega* **2021**, *6*, 21284−21293.
(13) Bandodkar, A. J.; Jeerapan, I.; Wang, J. Wearable Chemical Sensors: Present Challenges and Future Prospects. *ACS Sens.* **2016**, *1*, 464−482.
(14) Ding, Q.; Zhou, Z.; Wang, H.; Wu, Z.; Tao, K.; Yang, B. R.; Xie, X.; Fu, J.; Wu, J. Self-Healable, Recyclable, Ultrastretchable, and High-Performance NO2 Sensors Based on an Organohydrogel for Room and Sub-zero Temperature and Wireless Operation. *SmartMat* **2022**, *4*, No. e1141.
(15) Mansour, E.; Vishinkin, R.; Rihet, S.; Saliba, W.; Fish, F.; Sarfati, P.; Haick, H. Measurement of Temperature and Relative Humidity in Exhaled Breath. *Sens. Actuators, B* **2020**, *304*, No. 127371.
(16) Wang, D.; Zhang, D.; Mi, Q. A High-Performance Room Temperature Benzene Gas Sensor Based on CoTiO3 Covered TiO2 Nanospheres Decorated with Pd Nanoparticles. *Sens. Actuators, B* **2022**, *350*, No. 130830.
(17) Joshi, N.; Hayasaka, T.; Liu, Y.; Liu, H.; Oliveira, O. N.; Lin, L. A Review on Chemiresistive Room Temperature Gas Sensors Based on Metal Oxide Nanostructures, Graphene and 2D Transition Metal Dichalcogenides. *Microchim. Acta* **2018**, *185*, No. 213.
(18) Dey, A. Semiconductor Metal Oxide Gas Sensors: A Review. *Mater. Sci. Eng. B* **2018**, *229*, 206−217.
(19) Jung, G.; Hong, S.; Jeong, Y.; Shin, W.; Park, J.; Kim, D.; Lee, J.-H. Highly Selective and Low-Power Carbon Monoxide Gas Sensor Based on the Chain Reaction of Oxygen and Carbon Monoxide to Wo3. *ACS Appl. Mater. Interfaces* **2022**, *14*, 17950−17958.
(20) Jang, H.; Park, Y. J.; Chen, X.; Das, T.; Kim, M. S.; Ahn, J. H. Graphene-Based Flexible and Stretchable Electronics. *Adv. Mater.* **2016**, *28*, 4184−4202.
(21) Singh, E.; Singh, P.; Kim, K. S.; Yeom, G. Y.; Nalwa, H. S. Flexible Molybdenum Disulfide (MoS2) Atomic Layers for Wearable Electronics and Optoelectronics. *ACS Appl. Mater. Interfaces* **2019**, *11*, 11061−11105.
(22) Yang, Q.; Wang, Y.; Li, X.; Li, H.; Wang, Z.; Tang, Z.; Ma, L.; Mo, F.; Zhi, C. Recent Progress of Mxene-Based Nanomaterials in Flexible Energy Storage and Electronic Devices. *Energy Environ. Mater.* **2018**, *1*, 183−195.
(23) Duy, L. T.; Trung, T. Q.; Hanif, A.; Siddiqui, S.; Roh, E.; Lee, W.; Lee, N.-E. A Stretchable and Highly Sensitive Chemical Sensor Using Multilayered Network of Polyurethane Nanofibres with Self-Assembled Reduced Graphene Oxide. *2D Mater.* **2017**, *4*, No. 025062.
(24) Park, H. J.; Kim, W.-J.; Lee, H.-K.; Lee, D.-S.; Shin, J.-H.; Jun, Y.; Yun, Y. J. Highly Flexible, Mechanically Stable, and Sensitive NO2 Gas Sensors Based on Reduced Graphene Oxide Nanofibrous Mesh Fabric for Flexible Electronics. *Sens. Actuators, B* **2018**, *257*, 846−852.
(25) Zhang, H.; Zhang, D.; Zhang, B.; Wang, D.; Tang, M. Wearable Pressure Sensor Array with Layer-by-Layer Assembled Mxene Nanosheets/Ag Nanoflowers for Motion Monitoring and Human-Machine Interfaces. *ACS Appl. Mater. Interfaces* **2022**, *14*, 48907−48916.
(26) Wang, D.; Zhang, D.; Yang, Y.; Mi, Q.; Zhang, J.; Yu, L. Multifunctional Latex/Polytetrafluoroethylene-Based Triboelectric Nanogenerator for Self-Powered Organ-like Mxene/Metal-Organic Framework-derived CuO Nanohybrid Ammonia Sensor. *ACS Nano* **2021**, *15*, 2911−2919.
(27) Wang, D.; Zhang, D.; Chen, X.; Zhang, H.; Tang, M.; Wang, J. Multifunctional Respiration-driven Triboelectric Nanogenerator for Self-Powered Detection of Formaldehyde in Exhaled Gas and Respiratory Behavior. *Nano Energy* **2022**, *102*, No. 107711.
(28) Kumar, R.; Goel, N.; Hojamberdiev, M.; Kumar, M. Transition Metal Dichalcogenides-Based Flexible Gas Sensors. *Sens. Actuator, A* **2020**, *303*, No. 111875.
(29) Lee, G.; Zarei, M.; Wei, Q.; Zhu, Y.; Lee, S. G. Surface Wrinkling for Flexible and Stretchable Sensors. *Small* **2022**, *18*, No. e2203491.
(30) Guan, X.; Yu, Y.; Hou, Z.; Wu, K.; Zhao, H.; Liu, S.; Fei, T.; Zhang, T. A Flexible Humidity Sensor Based on Self-supported Polymer Film. *Sens. Actuators, B* **2022**, *358*, No. 131438.
(31) Punetha, D.; Kar, M.; Pandey, S. K. A New Type Low-Cost, Flexible and Wearable Tertiary Nanocomposite Sensor for Room Temperature Hydrogen Gas Sensing. *Sci. Rep.* **2020**, *10*, No. 2151.
(32) Yin, F.; Yue, W.; Li, Y.; Gao, S.; Zhang, C.; Kan, H.; Niu, H.; Wang, W.; Guo, Y. Carbon-Based Nanomaterials for the Detection of Volatile Organic Compounds: A Review. *Carbon* **2021**, *180*, 274−297.
(33) Ma, C.; Ma, M. G.; Si, C.; Ji, X. X.; Wan, P. Flexible Mxene-based Composites for Wearable Devices. *Adv. Funct. Mater.* **2021**, *31*, No. 2009524.
(34) Lee, W.; Park, H.; Kim, S. Y.; Park, S. M.; Kim, D. H.; Lee, H. Wireless-Powered VOCs Sensor Based on Energy-Harvesting Metamaterial. *Adv. Electron. Mater.* **2021**, *7*, No. 2001240.
(35) Fernandes, L. C.; Correia, D. M.; Pereira, N.; Tubio, C. R.; Lanceros-Méndez, S. Highly Sensitive Humidity Sensor Based on Ionic Liquid−Polymer Composites. *ACS Appl. Polym. Mater.* **2019**, *1*, 2723−2730.

https://doi.org/10.1021/acsami.3c02570
ACS Appl. Mater. Interfaces 2023, 15, 26138−26147

(36) Mishra, K.; Devi, N.; Siwal, S. S.; Zhang, Q.; Alsanie, W. F.; Scarpa, F.; Thakur, V. K. Ionic Liquid-Based Polymer Nanocomposites for Sensors, Energy, Biomedicine, and Environmental Applications: Roadmap to the Future. *Adv. Sci.* **2022**, *9*, No. e2202187.
(37) Pei, Y.; Zhang, Y.; Ma, J.; Fan, M.; Zhang, S.; Wang, J. Ionic Liquids for Advanced Materials. *Mater. Today Nano* **2022**, *17*, No. 100159.
(38) Kim, Y.; Lee, D.; Seong, J.; Bak, B.; Choi, U. H.; Kim, J. Ionic Liquid-Based Molecular Design for Transparent, Flexible, and Fire-Retardant Triboelectric Nanogenerator (Teng) for Wearable Energy Solutions. *Nano Energy* **2021**, *84*, No. 105925.
(39) Son, Y. J.; Bae, J. W.; Lee, H. J.; Bae, S.; Baik, S.; Chun, K.-Y.; Han, C.-S. Humidity-Resistive, Elastic, Transparent Ion Gel and Its Use in a Wearable, Strain-Sensing Device. *J. Mater. Chem. A* **2020**, *8*, 6013−6021.
(40) Jin, M. L.; Park, S.; Kim, J. S.; Kwon, S. H.; Zhang, S.; Yoo, M. S.; Jang, S.; Koh, H. J.; Cho, S. Y.; Kim, S. Y.; et al. An Ultrastable Ionic Chemiresistor Skin with an Intrinsically Stretchable Polymer Electrolyte. *Adv. Mater.* **2018**, *30*, No. e1706851.
(41) Kammakakam, I.; Bara, J. E.; Jackson, E. M.; Lertxundi, J.; Mecerreyes, D.; Tomé, L. C. Tailored Co2-Philic Anionic Poly(Ionic Liquid) Composite Membranes: Synthesis, Characterization, and Gas Transport Properties. *ACS Sustainable Chem. Eng.* **2020**, *8*, 5954−5965.
(42) Zhi, H.; Gao, J.; Feng, L. Hydrogel-Based Gas Sensors for NO2 and NH3. *ACS Sens.* **2020**, *5*, 772−780.
(43) Yol Jeong, S.; Jeong, S. Y.; Jeong, S.; Won Lee, S.; Tae Kim, S.; Kim, D.; Jin Jeong, H.; Tark Han, J.; Baeg, K.-J.; Yang, S.; Seok Jeong, M. S.; Lee, G. W. Enhanced Response and Sensitivity of Self-Corrugated Graphene Sensors with Anisotropic Charge Distribution. *Sci. Rep.* **2015**, *5*, No. 11216.
(44) Branco, A.; Branco, L. C.; Pina, F. Electrochromic and Magnetic Ionic Liquids. *Chem. Commun.* **2011**, *47*, 2300−2302.
(45) Li, L.; Zhu, G.; Wang, J.; Chen, J.; Zhao, G.; Zhu, Y. A Flexible and Ultrasensitive Interfacial Iontronic Multisensory Sensor with an Array of Unique "Cup-Shaped" Microcolumns for Detecting Pressure and Temperature. *Nano Energy* **2023**, *105*, No. 108012.
(46) Wang, J.; Cui, X.; Song, Y.; Chen, J.; Zhu, Y. Flexible Iontronic Sensors with High-Precision and High-Sensitivity Detection for Pressure and Temperature. *Compos. Commun.* **2023**, *39*, No. 101544.
(47) Jeyapandian, M.; Lavina, S.; Thayumanasundaram, S.; Ohno, H.; Negro, E.; Di Noto, V. New Hybrid Inorganic−Organic Polymer Electrolytes Based on Zr(O(Ch2)3ch3)4, Glycerol and Emim-Tfsi Ionic Liquid. *J. Power Sources* **2010**, *195*, 341−353.
(48) Höfft, O.; Bahr, S.; Kempter, V. Investigations with Infrared Spectroscopy on Films of the Ionic Liquid [EMIM]Tf2N. *Langmuir* **2008**, *24*, 11562−11566.
(49) Kiefer, J.; Fries, J.; Leipertz, A. Experimental Vibrational Study of Imidazolium-Based Ionic Liquids: Raman and Infrared Spectra of 1-Ethyl-3-Methylimidazolium Bis(Trifluoromethylsulfonyl)Imide and 1-Ethyl-3-Methylimidazolium Ethylsulfate. *Appl. Spectrosc.* **2007**, *61*, 1306−1311.
(50) Pullagura, B. K.; Amarapalli, S.; Gundabala, V. Coupling Electrohydrodynamics with Photopolymerization for Microfluidics-Based Generation of Polyethylene Glycol Diacrylate (PEGDA) Microparticles and Hydrogels. *Colloids Surf., A* **2021**, *608*, No. 125586.
(51) D'Angelo, A. J.; Panzer, M. J. Enhanced Lithium Ion Transport in Poly(Ethylene Glycol) Diacrylate-Supported Solvate Ionogel Electrolytes via Chemically Cross-Linked Ethylene Oxide Pathways. *J. Phys. Chem. B* **2017**, *121*, 890−895.
(52) Skorikova, G.; Rauber, D.; Aili, D.; Martin, S.; Li, Q.; Henkensmeier, D.; Hempelmann, R. Protic Ionic Liquids Immobilized in Phosphoric Acid-Doped Polybenzimidazole Matrix Enable Polymer Electrolyte Fuel Cell Operation at 200°C. *J. Membr. Sci.* **2020**, *608*, No. 118188.
(53) Murray, B. J.; Walter, E. C.; Penner, R. M. Amine Vapor Sensing with Silver Mesowires. *Nano Lett.* **2004**, *4*, 665−670.
(54) Wei, Y.; Wang, H.; Ding, Q.; Wu, Z.; Zhang, H.; Tao, K.; Xie, X.; Wu, J. Hydrogel- and Organohydrogel-Based Stretchable, Ultrasensitive, Transparent, Room-Temperature and Real-Time NO2 Sensors and the Mechanism. *Mater. Horiz.* **2022**, *9*, 1921−1934.
(55) Wu, Z.; Wang, H.; Ding, Q.; Tao, K.; Shi, W.; Liu, C.; Chen, J.; Wu, J. A Self-Powered, Rechargeable, and Wearable Hydrogel Patch for Wireless Gas Detection with Extraordinary Performance. *Adv. Funct. Mater.* **2023**, No. 2300046.
(56) Nallon, E. C.; Schnee, V. P.; Bright, C. J.; Polcha, M. P.; Li, Q. Discrimination Enhancement with Transient Feature Analysis of a Graphene Chemical Sensor. *Anal. Chem.* **2016**, *88*, 1401−1406.
(57) Acharyya, S.; Jana, B.; Nag, S.; Saha, G.; Guha, P. K. Single Resistive Sensor for Selective Detection of Multiple Vocs Employing SnO2 Hollowspheres and Machine Learning Algorithm: A Proof of Concept. *Sens. Actuators, B* **2020**, *321*, No. 128484.
(58) Le, Q. T.; Shikoh, A. S.; Kang, K.; Lee, J.; Kim, J. Room-Temperature Sub-Ppm Detection and Machine Learning-Based High-Accuracy Selective Analysis of Ammonia Gas Using Silicon Vertical Microwire Arrays. *ACS Appl. Electron. Mater.* **2023**, *5*, 357−366.
(59) Spector, N. H. Alcohol Breath Tests: Gross Errors in Current Methods of Measuring Alveolar Gas Concentrations. *Science* **1971**, *172*, 57−59.
(60) Liang, C.; Yuan, C.-Y.; Warmack, R. J.; Barnes, C. E.; Dai, S. Ionic Liquids: A New Class of Sensing Materials for Detection of Organic Vapors Based on the Use of a Quartz Crystal Microbalance. *Anal. Chem.* **2002**, *74*, 2172−2176.
(61) Yuan, W. L.; Yang, X.; He, L.; Xue, Y.; Qin, S.; Tao, G. H. Viscosity, Conductivity, and Electrochemical Property of Dicyanamide Ionic Liquids. *Front. Chem.* **2018**, *6*, No. 59.
(62) Seddon, K. R.; Stark, A.; Torres, M.-J. Influence of Chloride, Water, and Organic Solvents on the Physical Properties of Ionic Liquids. *Pure Appl. Chem.* **2000**, *72*, 2275−2287.
(63) Ehbrecht, M.; Huisken, F. Vibrational Spectroscopy of Ethanol Molecules and Complexes Selectively Prepared in the Gas Phase and Adsorbed on Large Argon Clusters. *J. Phys. Chem. A* **1997**, *101*, 7768−7777.
(64) Barthel, J.; Buchner, R.; Wismeth, E. FTIR Spectroscopy of Ion Solvation of LiClO4 and LiSCN in Acetonitrile, Benzonitrile, and Propylene Carbonate. *J. Solution Chem.* **2000**, *29*, 937−954.
(65) Barthel, J.; Deser, R. Ftir Study of Ion Solvation and Ion-Pair Formation in Alkaline and Alkaline Earth Metal Salt Solutions in Acetonitrile. *J. Solution Chem.* **1994**, *23*, 1133−1146.

https://doi.org/10.1021/acsami.3c02570
ACS Appl. Mater. Interfaces 2023, 15, 26138−26147